The effect of temperature and time on the properties of 2D Cs2ZnBr4 perovskite nanocrystals and its application in a Schottky barrier device

9 authors, including:

Olusola Akinbami
University of the Witwatersrand
5 PUBLICATIONS **6** CITATIONS

SEE PROFILE

Grace Ngubeni
University of the Witwatersrand
8 PUBLICATIONS **24** CITATIONS

SEE PROFILE

Francis Otieno
University of the Witwatersrand
20 PUBLICATIONS **93** CITATIONS

SEE PROFILE

Ella Cebisa Linganiso
University of the Witwatersrand
25 PUBLICATIONS **148** CITATIONS

SEE PROFILE

Some of the authors of this publication are also working on these related projects:

Colloidal nanostructures View project

Feasibility studies of commercial waste to energy plants View project

ROYAL SOCIETY
OF CHEMISTRY

PAPER

Check for updates

The effect of temperature and time on the properties of 2D Cs$_2$ZnBr$_4$ perovskite nanocrystals and their application in a Schottky barrier device†

O. Akinbami,[a] G. N. Ngubeni,[a] F. Otieno,[ab] R. Kadzutu-Sithole,[a] E. C. Linganiso,[acd] Z. N. Tetana,[acd] S. S. Gqoba,[a] K. P. Mubiayi*[ac] and N. Moloto ✦ *[a]

2D hybrid perovskites are promising materials for solar cell applications, in particular, cesium-based perovskite nanocrystals as they offer the stability that is absent in organic−inorganic perovskites. However, the most commonly studied are the lead halides and the toxicity of lead has come under much scrutiny. Cs$_2$ZnBr$_4$ is a less studied Cs-based perovskite that is less toxic than lead halides, offers higher stability than the organic−inorganic perovskites, and has optoelectronic properties suitable for application in solar cells. Herein, we report the colloidal synthesis of Cs$_2$ZnBr$_4$ nanocrystals for the first time. We studied their properties by varying the temperature and time. We then used these resultant nanocrystals in a Schottky diode. Varying the temperature and time resulted in a change in particle size and morphology. These inevitably resulted in different optical properties. The optimum temperature and time were 160 °C and 1 min. The surface chemistry of the nanocrystals was studied using XPS, FT-IR, and NMR techniques. This confirmed that the nanocrystals were capped by oleylamine. The nanocrystals were still stable for 25 days, as confirmed by XRD and TGA. From the Schottky barrier diode, the ideality factor values, barrier heights, and series resistances were determined using the traditional thermionic emission theory of a Schottky barrier, the modified Cheung's and Norde's functions. Notably, high ideality factor values were obtained suggesting poor interface properties. Nevertheless, the optical properties, saturation current and the rectification of the I−V curve suggest that Cs$_2$ZnBr$_4$ nanocrystals are good candidates for use as hole or electron transporting layers in solar cells.

1. Introduction

Ever since high efficiencies were observed in hybrid perovskite solar cells, solar cells and materials have remained at the forefront of research. Efficiencies greater than 20% have been reported and central to these are organic–inorganic perovskites.[1,2] However, hampering the progress of these solar cells has been the stability of materials.[3] This has perpetuated new efforts into the research of alternative perovskite materials that can achieve similar efficiencies while being stable over long periods of time. Research into all-inorganic perovskites has thus been pursued.

Among the most studied are the Cs-based hybrid perovskite nanocrystals. Cs-based nanocrystals are the most studied due to the optimum ionic radius of Cs and its stability.[4] In an effort to further improve the properties of Cs-based nanocrystals, studies that vary the B cation and the halides have been undertaken. CsPbI$_3$ under optimized conditions has shown 21.31% efficiency.[5] While the use of lead has led to great efficiencies, its toxicity has come under major scrutiny. This has led to the exploration of other B ions. Tin, bismuth, and zinc have been recently studied.[6] Herein, we report on the use of Zn as the B atom for the synthesis of Cs-based hybrid perovskite nanocrystals. Unlike Pb, Zn is an essential element required for the proper physiological functioning of the human body, as such, it is less toxic.[7] The exploration of Zn as a potential substitute for Pb was further informed by earlier studies on Zn incorporation into perovskites. For instance, the all-inorganic CsPbIBr$_2$ was doped with ZnBr$_2$; the doped perovskite showed improved stability and crystallinity, where just 1% ZnBr$_2$ doping improved the power conversion efficiency of the device by 34%.[8] Also, the CsPb$_{0.99}$Zn$_{0.01}$IBr$_2$ device showed superior long-term stability under ambient conditions and against heat. In another study,

[a] *Molecular Sciences Institute, School of Chemistry, University of the Witwatersrand, Private Bag 3, Wits, 2050, South Africa. E-mail: Kalenga.Mubiayi@wits.ac.za, Nosipho.Moloto@wits.ac.za; Tel: +2711 717 6720, +2711 717 6774*

[b] *Department of Physics, University of the Witwatersrand, Private Bag 3, Wits, 2050, Republic of South Africa*

[c] *DSI/NRF Centre of Excellence in Strong Materials, University of the Witwatersrand, Private Bag 3, Wits 2050, South Africa*

[d] *Microscopy and Microanalysis Unit, University of the Witwatersrand, Private Bag 3, Johannesburg, Wits 2050, South Africa*

† Electronic supplementary information (ESI) available. See DOI: 10.1039/d1tc00264c

PbI_2 was substituted with $ZnCl_2$ in $CH_3NH_3PbI_3$; upon the introduction of $ZnCl_2$, the film morphology improved while the power conversion efficiency of the device increased from 16.4% to 18.2%.[9] The device that contained $ZnCl_2$ showed improved stability under ambient conditions when compared to the undoped device. Lastly, the incorporation of Zn into $CsPbCl_3$ reportedly improved the overall photoluminescence quantum yield of the perovskite while also exhibiting impressive moisture- and photo-stability.[10]

2D hybrid perovskites (so-called Ruddlesden–Popper), unlike traditional perovskites such as $CaTiO_3$ that take on the ABX_3 formula with A having an oxidation state +2, B +4, and X −2, have been shown to take on varied oxidation states. 2D hybrid perovskites have become promising semiconductors due to their high degree of structural flexibility and tunable optoelectronic properties.[11] They have a general formula of $A_{n+1}B_nX_{3n+1}$, where A = Cs^+, $CH_3NH_3^+$ (MA), $HC(NH_2)_2^+$ (FA), B = Ge^{2+}, Sn^{2+}, Pb^{2+} and X = Cl^-, Br^-, I^- and n can be n = 1, 2, 3, 4, 5.[12–15] 2D hybrid perovskites are generally synthesized from the bottom-up self-assembly of individual, semiconducting perovskite sheets having an adjustable slab thickness of up to a few nanometers.[16] Only recently has B = Zn^{2+} been investigated following structural determination in 1959.[17] Cheng *et al.* and Zhu *et al.* reported on the syntheses of OD-doped cesium zinc halide nanocrystals. The OD structures in these studies refer to the morphologies of nanocrystals and the confinement of density of states rather than the crystal structure.[18,19]

Herein, we investigate the synthesis of Cs_2ZnBr_4 using the colloidal method. Furthermore, we investigate the effect of changing the reaction temperature and time on the properties of Cs_2ZnBr_4. The variation of temperature and time in the colloidal synthesis follows the Lamer and Dinegar mechanism.[20] An increase in temperature and time promotes the growth of the nuclei through Ostwald ripening. Apart from the size, the temperature has been shown to also greatly affect the morphology, crystal structure, and phase of nanocrystals.[21,22] Perovskite nanocrystals have of course been excellent materials for solar cell applications. A solar cell is effectively a diode under illumination. As such, herein, we study the diode behavior of Cs_2ZnBr_4 nanocrystals by fabricating a Schottky barrier device. Schottky barrier devices involve a metal-semiconductor junction and result in diode behavior. Solar cell performances are generally influenced by interfacial interactions between different layers. More prudent is the metal-semiconductor layer. The Schottky diode can give useful information about the interface such as the ideality factor, barrier height as well as resistance, all of which give insight into the electrical properties of the semiconductor material.

2. Experimental section

Chemicals

Zinc bromide ($ZnBr_2$, 99%), cesium carbonate (Cs_2CO_3, 99%), oleylamine (OLA, 70%), oleic acid (OA, 90%), toluene (95%), and dichloromethane (anhydrous > 99.8%) were purchased from Sigma-Aldrich. All chemicals were used without any further purification.

Synthesis of Cs_2ZnBr_4 nanocrystals

Under nitrogen flow, 0.1 g cesium carbonate (Cs_2CO_3) was placed in 7 mL of oleic acid (OA) in a three-necked round bottom flask and heated to 140 °C for 1 h under vigorous stirring for Cs_2CO_3 to completely dissolve and form a cesium oleate (CsOA) stock solution. In a separate 25 mL three-necked flask, 0.3 g zinc bromide ($ZnBr_2$) was placed in an equal volume (7.5 mL) of OA and oleylamine (OLA) and heated to 160 °C for 1 h for $ZnBr_2$ to completely dissolve. Thereafter, 1 mL of CsOA was swiftly injected into a three-necked flask containing $ZnBr_2$ with a syringe, where, after 1 min, the flask was cooled to room temperature using a cold-water bath. The resultant powders were collected through centrifugation and subsequently washed in ethanol/toluene solution. Following the same method, the temperature and time were varied.

Fabrication of Schottky diode

The device structure consists of the following film layers: ITO/Cs_2ZnBr_4/Au. The Cs_2ZnBr_4 layer was spin-coated onto an ITO substrate. About 50 μL of a toluene solution containing Cs_2ZnBr_4 NPs was dispersed on the substrate, spun at 3000 rpm, and allowed to dry forming a thin film coating. The top Au contact was thermally deposited through a shadow mask to generate an array of patterned electrodes. Au was deposited in a high vacuum of better than 4×10^{-5} Pa, the voltage of 80 kV, current of 280 A for 5 min with the device having an active area of 0.05 cm^2 (Fig. 1).

Characterization

Powder X-ray diffraction (PXRD) analysis was conducted using a Bruker D2 phaser (D2-205530) diffractometer using a Cu Kα radiation source (λ 1.541060 Å) at 30 kV and 10 mA. The measurements were taken over the range of 5 to 90° at room temperature. The morphologies were determined using an FEI Technai T12 Transmission Electron Microscope (TEM), operated at 120 kV with a beam spot of 3 in the TEM mode. The nanocrystals were dispersed in toluene and drop-casted onto a lacey-carbon copper grid and dried at room temperature before analysis. The absorption measurements were done by dispersing the nanoparticles in toluene and then placed into a quartz cuvette (1 cm path length), thereafter the measurements were
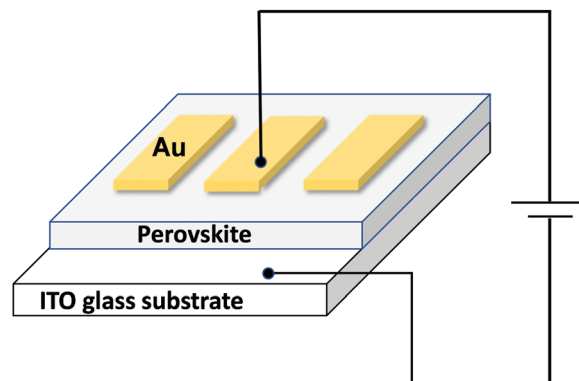

Fig. 1 Schematic showing the device architecture of the Schottky diode.

carried out on a Specord 210 AnalytikJena UV-vis spectrophotometer. The photoluminescence measurements on powdered samples were performed using a HORIBA QM8000 spectrofluorometer equipped with a PPD-850 detector. X-ray photoelectron spectroscopy (XPS) analysis was conducted using a Physical Electronics PHI 5700 spectrometer using non-monochromatic Mg $K\alpha$ x-rays (300 W, 15 kV, and 1253.6 eV) as the excitation source. The spectrometer energy scale was calibrated using Cu $2p_{3/2}$, Ag $3d_{5/2}$, and Au $4f_{7/2}$ photoelectron lines at 932.7, 368.3, and 84.0 eV, respectively. Samples were mounted on a sample holder without adhesive tape and kept overnight at a high vacuum in the preparation chamber before being transferred to the analysis chamber for testing. The spectra were collected in the constant pass energy mode at 29.35 eV. The residual pressure in the analysis chamber was maintained below 1.33×10^{-7} Pa during the spectra acquisition. FT-IR spectra were measured on a Bruker Tensor 27 FT-IR and the nuclear magnetic resonance (NMR) data were obtained using a 500 MHz Bruker AVANCE III; the samples were run using $CDCl_3$ as a solvent at room temperature. The I–V measurement for the Schottky device was performed in the dark at 298 K using a Keithley 2400 source meter.

3. Results and discussion

Powder X-ray diffraction was used to determine the crystal phases of the resultant nanocrystals and for the detection of any impurities. Shown in Fig. 2 are the PXRD patterns of the nanocrystals synthesized at different temperatures and the reference pattern of Cs_2ZnBr_4. PXRD patterns matched those of Cs_2ZnBr_4 and crystallized in the orthorhombic phase with a reference card number PDF 01-088-2355 and lattice parameters: a = 10.202 Å, b = 7.738 Å, and c = 13.5390 Å. The space group of the synthesized nanocrystals was *Pnma* (62), indicating that nanocrystals belonged to the D_{2h} point group.[23] The peaks in PXRD patterns of the synthesized materials were all assigned to the reference peaks indicating the phase purity of Cs_2ZnBr_4. Fig. 2 also shows that the peak intensity increases with an increase in the temperature. This is indicative of an increase in the crystallinity of the nanocrystals.

TEM was used to determine the morphology of the particles as the temperature was increased from 160 °C to 220 °C. As evident from images in Fig. 3, there was an increase in the size of the nanocrystals with increasing reaction temperature from an average aspect ratio of 2 to 3 for 160 °C and 190 °C, respectively. However, the aspect ratio was reduced to 2.5 at 220 °C. Small nanorods with average lengths of 30.8 nm and widths of 17.6 nm were produced at 160 °C reaction temperature (see Fig. S1, ESI† for higher magnification), while bigger nanorods with average lengths of 138.7 nm and width of 48.4 nm were produced at 190 °C. The reduction in the aspect ratio observed at the higher temperature (beyond 200 °C) was due to the widening of nanocrystals. From 160 °C to 190 °C, there was a preferential growth in the lengths of the nanocrystals, but at 220 °C, growth along the widths of the nanocrystals was preferred. The nanorods at 160 °C were comparatively smaller and more
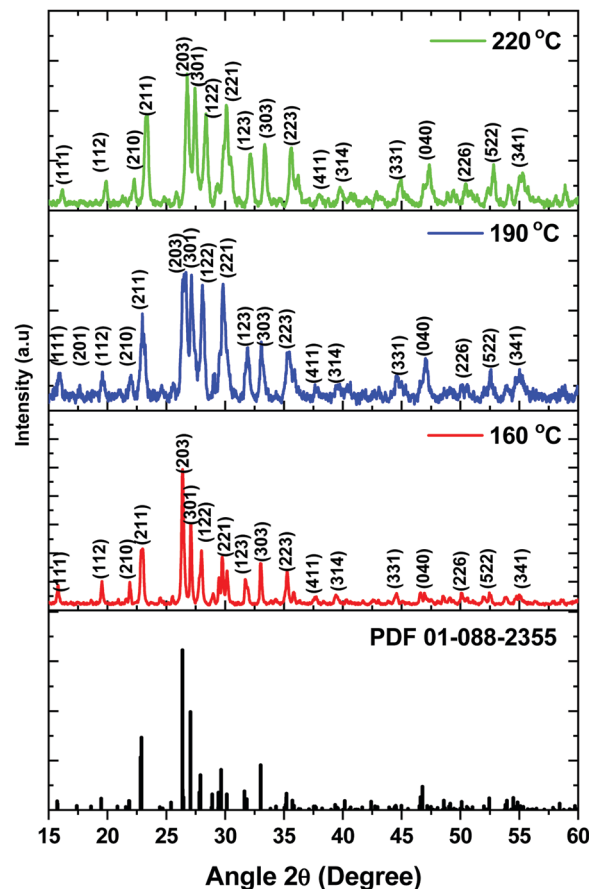

Fig. 2 XRD patterns of Cs_2ZnBr_4 nanocrystals synthesized at different temperatures.

monodispersed, at a much lower temperature since the ligands are more strongly bonded on the nanocrystals thus influencing their growth as compared to the nanocrystals synthesized at higher temperatures, where the thermal agitation weakens the surfactant binding to the nanocrystals.[24]

The optical properties of a material are crucial in optoelectronic applications. It has been shown that the size, shape, and dispersity of nanocrystals can influence the optical properties, as a result of the quantum confinement effects and density of states in the nanocrystals.[25,26]

The optical properties of Cs_2ZnBr_4 nanocrystals synthesized at different temperatures were studied using UV-vis absorption and photoluminescence spectroscopy and the results are depicted in Fig. 4. From the Tauc plots (corresponding absorption spectra shown in Fig. S2, ESI†), a decrease in band-gap was observed as the temperature was increased from 3.18 eV, 2.96 eV to 2.60 eV for 160 °C, 190 °C, and 220 °C, respectively. This was attributed to an increase in particle sizes due to Ostwald ripening effects brought about by the increase in temperature.[27] The Ostwald ripening effect is a growth process whereby smaller nanocrystals possessing high solubility and surface energy redissolve in a solution causing larger particles to grow even further.[28–30] This process is influenced by heating since at high temperatures, ample energy is introduced into the system resulting in an effective collision necessary for
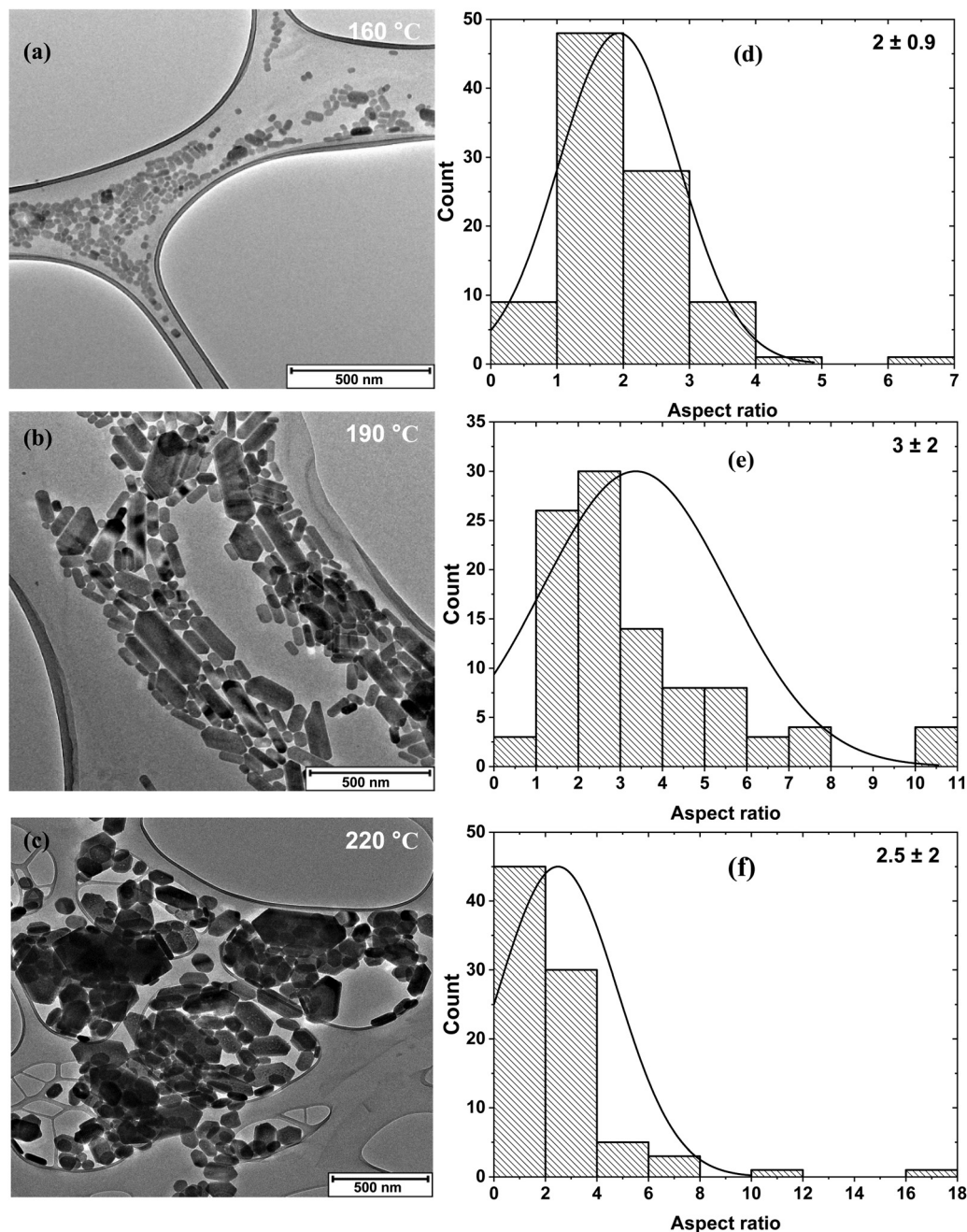
Fig. 3 (a–c) TEM images and (d–f) corresponding size distribution of Cs_2ZnBr_4 nanocrystals synthesized at different temperatures.

surface atom diffusion that is required for Ostwald ripening.[31,32] The bandgap energy of a semiconductor is strongly dependent on the nanocrystal's size because the spacing of electronic energy levels increases with a decrease in the nanocrystallite size.[33–35] The photoluminescence spectrum is typically red-shifted from the UV-vis absorption spectrum due to radiative losses and other defects. The emission maxima for particles synthesized at 160 °C, 190 °C and 220 °C were 2.85 eV, 2.82 eV, and 2.73 eV, respectively. The 160 °C and 190 °C emission maxima were red-shifted from the absorption band-gaps as expected, however, for 220 °C particles, the emission maximum was blue-shifted. The blue-shift was attributed to the higher degree of polydispersity

as observed in the TEM image, size distribution histogram and the broadness of the photoluminescence spectrum.

The effect of time on the properties of nanocrystals has been well studied.[23,24] However, to our knowledge, no work has been reported on the effect of time on the properties of Cs_2ZnBr_4 nanocrystals. Shown in Fig. 5 are XRD patterns of Cs_2ZnBr_4 synthesized at different times. The nanocrystals form rapidly as shown, and within a minute all the peaks could be indexed to orthorhombic Cs_2ZnBr_4 (PDF 01-088-2355). As the time was prolonged to 5 min, no changes in the crystal structure were observed. However, extending the time further (10 min) resulted in the formation of tetragonal Cs_3ZnBr_5 (PDF 00-066-0032).
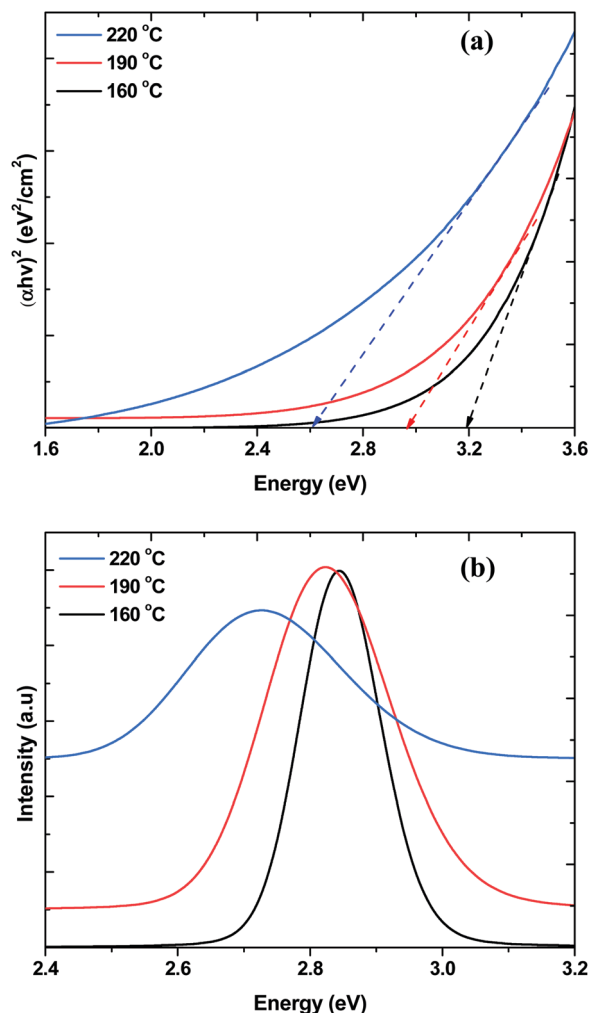
Fig. 4 (a) Tauc plots derived from UV-vis absorption spectra and (b) photoluminescence spectra of Cs_2ZnBr_4 nanocrystals synthesized at different temperatures.

Fig. 5 XRD patterns of Cs_2ZnBr_4 nanocrystals synthesized at different times.

The morphology and size of Cs_2ZnBr_4 nanocrystals changed drastically with increasing time. As shown in Fig. 6, an obvious increase in the size of the nanocrystals was observed with increasing reaction time. Smaller nanorods with an aspect ratio of (average length of 38 nm and a width of 22 nm) were produced in 1 min of reaction time (higher magnification image is shown in Fig. S1, ESI†), while bigger rods with an aspect ratio of 3 (average length of 366 nm and a width of 131 nm) were produced in 10 min of reaction time. This continuous growth in nanocrystal size was due to the Ostwald ripening effect whereby larger particles are formed at the expense of small ones since the smaller ones are more soluble than larger ones. Therefore, as time progresses in the synthesis of Cs_2ZnBr_4, smaller particles diffuse and deposit on the larger particles. Similar Ostwald ripening processes have been reported in the synthesis of perovskites.[36–38]

The optical properties of Cs_2ZnBr_4 synthesized at different times are depicted in Fig. 7 (corresponding absorption spectra are shown in Fig. S2, ESI†). The 1 min sample had a band-gap of 3.18 eV; this is the same sample that is shown in Fig. 4 as the
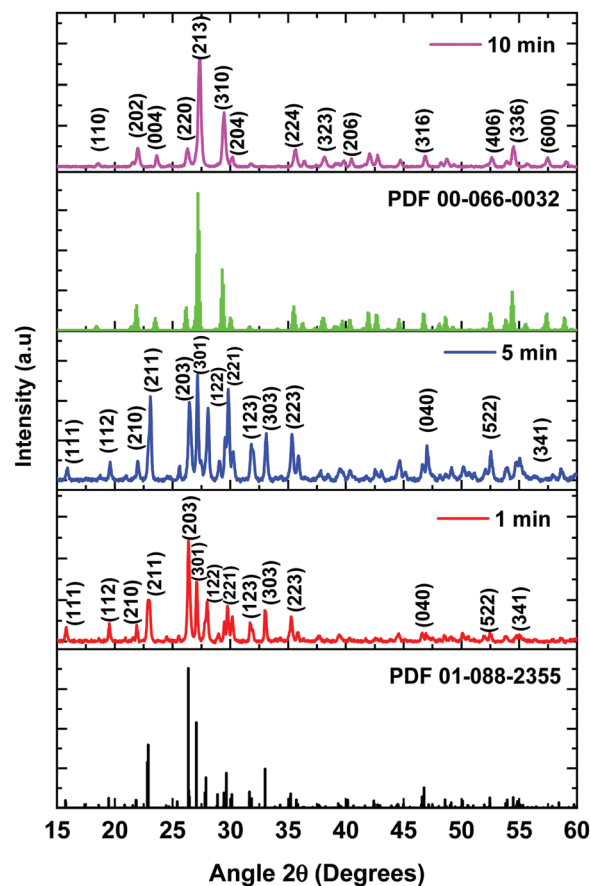
reaction conditions were the same. As time was increased to 5 min and 10 min, there was a decrease in band-gap, consistent with an increase in particle size. The band-gaps were 2.60 eV and 2.32 eV for 5 min and 10 min samples, respectively. Photoluminescence spectra showed a red-shift in the energy with time. Also, large FWHM were observed for the 5 and 10 min samples, signifying polydispersed samples and this is consistent with the TEM images shown in Fig. 6.

From the obtained results discussed above, it is apparent that the particles synthesized at 160 °C for 1 min gave the best results. The particles were more monodispersed, and much smaller and no impurities were detected in the XRD pattern. This sample was therefore further studied, especially its surface chemistry as it influences its processability and applicability. The surface of the nanocrystals is thought to be capped with a layer of surfactant molecules and in this case, they were oleic acid and oleylamine. This is a common assumption in the colloidal synthesis of nanocrystals. The survey spectrum of the capped Cs_2ZnBr_4 is shown in Fig. S3 (ESI†) and Br 3d, C 1s, N 1s, O 1s, Cs 3d, and Zn 2p were detected. These data are consistent with those of OA/OLA capped Cs_2ZnBr_4. Shown in Fig. 8 are the high-resolution spectra of capped Cs_2ZnBr_4 nanocrystals synthesized at 160 °C for 1 min. The C 1s spectrum was deconvoluted into three peaks corresponding to C–C, C–O, and O–C≡O bonding.
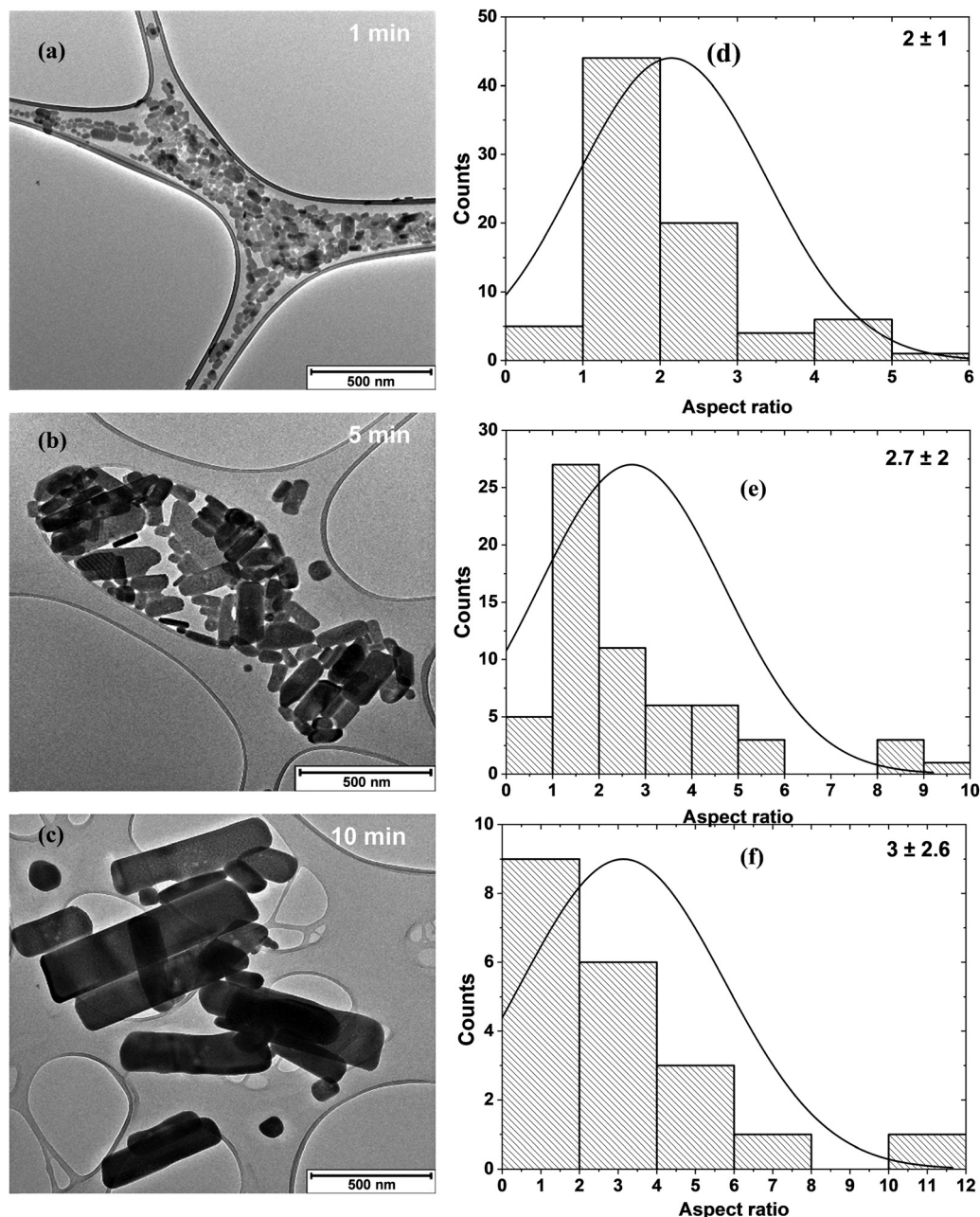
Fig. 6 (a–c) TEM images and (d–f) corresponding size distribution of Cs_2ZnBr_4 nanocrystals synthesized at different times.

The presence of C–C was to be expected and was attributed to long alkyl-chains of the capping agents. C–O and O–C=O were indicative of OA capping, however, it must be noted that the capping agent is prone to oxidation.[39] The N 1s and O 1s high-resolution spectra are shown in Fig. S3 (ESI†). The N 1s peak at 401.6 eV is likely due to the organometallic Zn complex formed as a result of interaction between $ZnBr_2$ and OLA,[40] while O 1s peak at 532.4 eV is due to organic O from OA used during the synthesis.[41] The atomic composition for both N and O was 3.3% and 3.9%, respectively, as shown in Table 1. The Cs 3d high-resolution spectrum showed two peaks at 725.8 eV and 739.9 eV corresponding to $3d_{5/2}$ and $3d_{3/2}$ of Cs^+. The Zn 2p high-resolution spectrum showed two peaks at 1025.2 eV and

1048.4 eV corresponding to $2p_{3/2}$ and $2p_{1/2}$, respectively. This is as a result of Zn^{+2} species being present. The high-resolution Br 3d spectrum was deconvoluted into three peaks at 69.0 eV ($3d_{5/2}$), 69.4 eV, and 69.8 eV ($3d_{3/2}$), where the peaks at 69.0 eV and 69.8 eV were due to $ZnBr_2$ bonding in the material,[42] while the deconvoluted peak at 69.4 eV was due to Cs-Br bonding.[43] The percentage compositions of the present species are shown in Table 1.

To further study the nature of the interaction of capping molecules with nanocrystals, FTIR and NMR studies were undertaken. The FTIR spectra are shown in Fig. S4 (ESI†) and results are summarized in Table 2. The OA spectrum showed all the expected bands with significant bands C–O and C=O
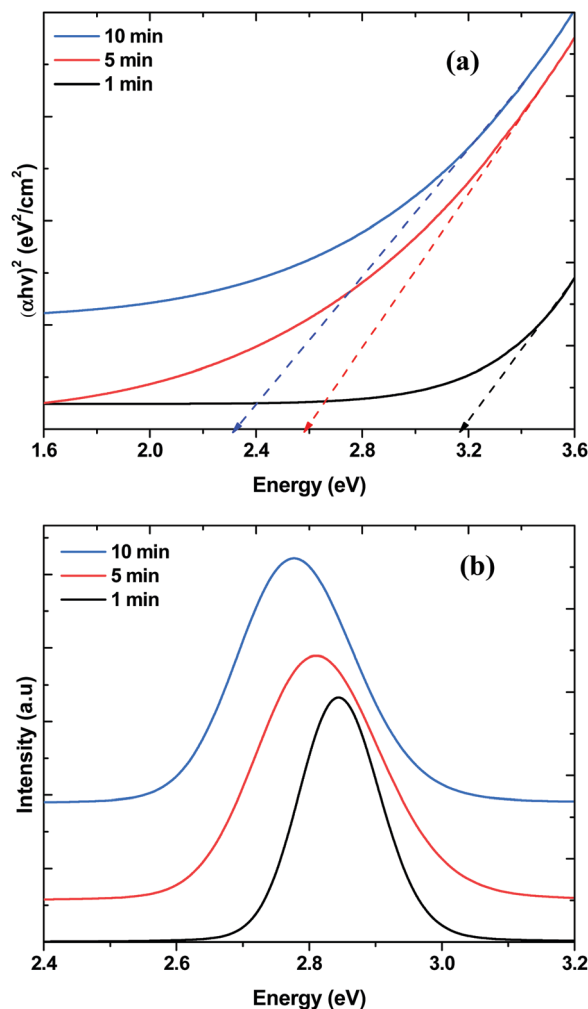
Fig. 7 (a) Tauc plots derived from UV-vis absorption spectra and (b) photoluminescence spectra of Cs_2ZnBr_4 nanocrystals synthesized at different times.

found at 1265 cm^{-1} and 1719 cm^{-1}, respectively. Cs_2ZnBr_4 nanocrystals are thought to be capped by both OA and OLA. From FTIR results, no C–O or C=O bands were observed in the Cs_2ZnBr_4 spectrum. The OLA spectrum showed all C–H and C=C bands and a weak N–H band at 1606 cm^{-1}. The N–H bands were significantly present in the Cs_2ZnBr_4 spectrum, thereby, suggesting that OLA was indeed capping the particles. The absence of the C=O band suggested that OA was not capping the nanocrystals. FTIR spectroscopy, while it is a useful technique it is however not conclusive.

To further elucidate on the capping, NMR spectroscopy was performed. The spectra are shown in Fig. S5 and S6 (ESI†) and the results are summarized in Table 3. From ^{1}H NMR and ^{13}C NMR, all protons and carbons were accounted for in OLA $(CH_3(CH_2)_7CH=CH(CH_2)_7CH_2NH_2$ and OA $(CH_3(CH_2)_7CH=CH(CH_2)_7COOH)$ spectra. The distinguishing peaks for OLA were –NH$_2$ (1.37–1.40 ppm) and –CH$_2$–NH$_2$ (2.61–2.64 ppm) chemical shifts in the proton spectrum and –CH$_2$–NH$_2$ (42.39 ppm) in the carbon spectrum. Contrary, to OA, –CH$_2$–C=O (2.33–2.36 ppm) chemical shifts in the proton spectrum and C=O

(180.46 ppm) chemical shifts in the carbon spectrum were the differentiating bands. On the other hand, the NMR results of the capped Cs_2ZnBr_4 were slightly compromised. Generally, it is thought that both OA and OLA are bounded to the surface of the nanocrystals as separate entities.[44] It is however possible for a condensation reaction between the carboxylic acid (OA) and amine (OLA) to form and result in a carboxylate salt as an intermediate before the formation of an amide as shown below:

Nevertheless, studying the ^{1}H NMR spectrum of Cs_2ZnBr_4 nanocrystals, strong toluene peaks were observed and these were impurities from the solvent used to wash and disperse the nanocrystals. Also observed were the triplet –CH$_2$ peaks at 1.97 ppm associated with methylene protons adjacent to ethylene protons (–CH$_2$–CH=CH–CH$_2$–) and the ethylene chemical shift at 5.50 ppm. However, more telling were the –CH$_2$–NH$_2$ (2.22–2.23 ppm) peaks, these peaks suggest that only OLA was capping the nanocrystals. Even when examining the ^{13}C NMR spectrum, no C=O peaks were observed, further suggesting that only OLA was capping the nanocrystals. This observation is consistent with FTIR results, where only N–H bands were observed in the Cs_2ZnBr_4 spectrum shown in Fig. S4 (ESI†). It is not completely unexpected that OLA will bind to the nanocrystals solely, as amines are better nucleophiles than acids. This further suggests that the O observed in the XPS was from the surface oxidation of OLA. Surface oxidation of a capping agent is readily observed in capped nanocrystals.[39] The nature of the surface of nanocrystals, especially for perovskite nanocrystals, is important for mainly two reasons; (1) the capping agent is known to stabilize nanocrystals, a property that is much sort after in perovskite nanocrystals, and (2) the surface affects the reactivity hence properties and applicability of nanocrystals.

Before the application of nanocrystals, stability studies were performed. The particles were stored at room temperature in a cool, dry cabinet prior to analysis while the stability studies were performed under ambient conditions. From XRD studies, the crystal structure and phase did not change over a period of 25 days and no decomposition products were detected (Fig. 9). In comparison, the model $CsPbBr_3$ has been shown to lose its properties over a matter of hours.[45] In addition to structural stability, TGA was performed to establish thermal stability. The particles were stable until 700 °C, thereafter a rapid decomposition was observed (Fig. 9). The stability suggests that 2D hybrid perovskite are better candidates for use in various applications.

So, here, Cs_2ZnBr_4 nanocrystals were used as the semiconductor in a Schottky diode. Shown in Fig. 1 is the device architecture with an active device area of 0.05 cm^2. The Schottky barrier height was measured from the I–V curve shown in Fig. 10. According to the Schottky thermionic theory the dependence of the forward current I on the applied voltage V is given by the relation:

$$I = I_0 \left[\exp\left(\frac{qV}{nkT}\right) - 1 \right] \tag{1}$$

where q is the electronic charge, k is the Boltzmann constant, T the ambient temperature, and n is a dimensionless factor indicating the deviation from the ideal Schottky cell characteristics.
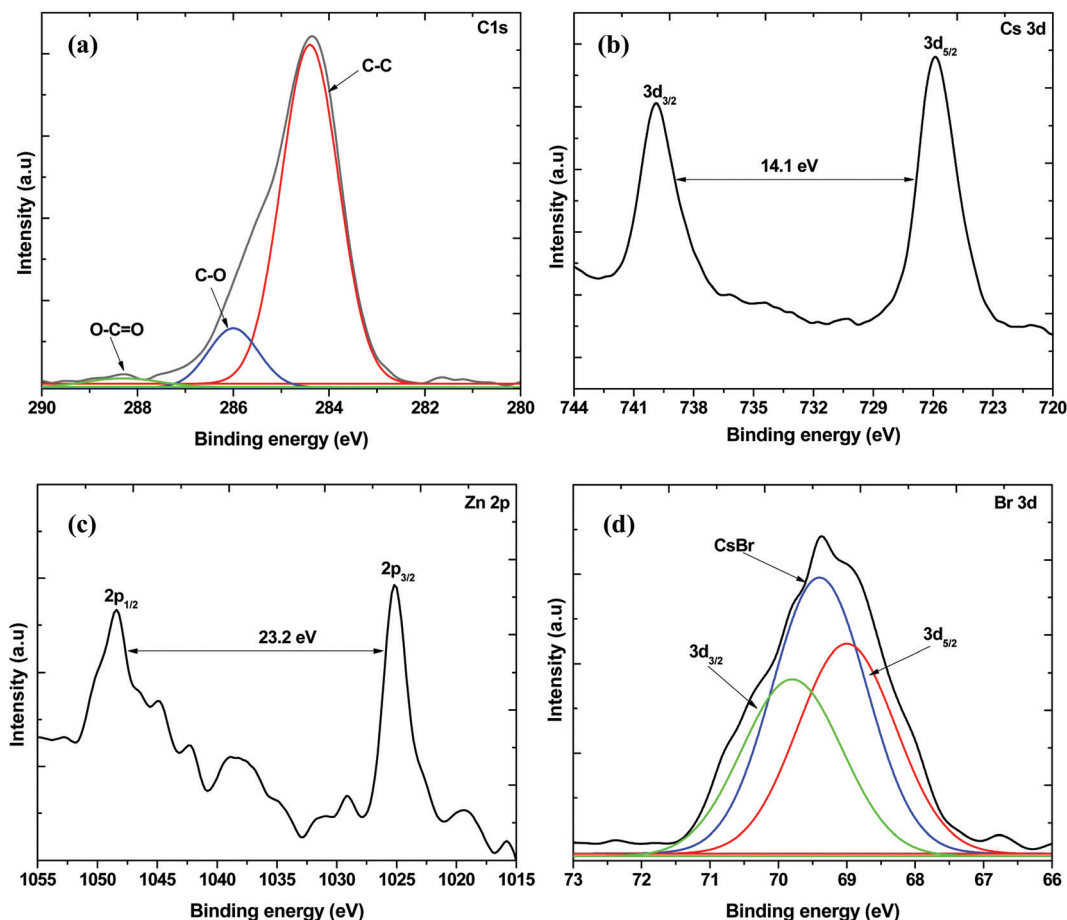
Fig. 8 XPS high-resolution spectra of Cs$_2$ZnBr$_4$ nanocrystals synthesized at 160 °C for 1 min showing (a) C 1s (b) Cs 3d (c) Zn 2p and (d) Br 3d spectra.

Table 1 Summary of the atomic composition and stoichiometric assignments obtained from the fitting of XPS spectra of Cs$_2$ZnBr$_4$ shown in Fig. S3 (ESI) and Fig. 8

Element	Peak binding energy (eV)	Atomic %	Assignment	Assignment binding energy (eV)	Assignment %
Br	69.0	16.1	Br 3d$_{5/2}$	69.0	32
			CsBr	69.4	40.5
			Br 3d$_{3/2}$	69.8	27.5
C	284.9	65.3	C–C	284.4	84.3
			C–O	286.0	12.9
			O–C=O	288.4	2.8
N	401.6	3.3	—	—	—
O	532.4	3.9	—	—	—
Cs	725.8	6.4	Cs 3d$_{5/2}$	725.9	60.0
			Cs 3d$_{3/2}$	739.7	40.0
Zn	1026.0	5.0	Zn 2p$_{3/2}$	1025.2	70.0
			Zn 2p$_{1/2}$	1048.4	30.0

This deviation arises from image force and surface effects such as surface charges and an interfacial dielectric layer between the metal and semiconductor.[46] I_0 is the saturation current represented by eqn (2):

$$I_0 = SA^*T^2 \exp\left(-\frac{q\varnothing_B}{kT}\right) \quad (2)$$

$$\text{Ln}I = \text{Ln}I_0 + \frac{q}{nkT}V \quad (3)$$

$$\varnothing_B = \left(-\frac{kT}{q}\right)\text{Ln}\left(-\frac{SA^*T^2}{I_0}\right) \quad (4)$$

with $A^* = A\left(\frac{m^*}{m_0}\right)$, where A is the Richardson constant ($A = 120 \text{ cm}^{-2} \text{ K}^{-2}$), m^* the effective electron mass is estimated to be $0.12 \, m_0$ for perovskite,[47] $\varnothing_B$ is the barrier height, and S the area of the cell. The coefficient n is evaluated from the slope of LnI *versus* V (eqn (3)), and the value $\varnothing_B$ is calculated from eqn (2). The saturation current and breakdown voltage were found to be 9.98 mA and 0.49 V, respectively. The n value was calculated from the slope and was found to be 9.63. The Schottky diode's ideality factor provides information about how closely the Schottky diode follows the ideal diode equation, wherein for an ideal diode, n is 1. However, due to extrinsic factors such as the presence of interface states or barrier height inhomogeneity, deviation from unity may occur.[48] The high value of n was due in part to defects induced by cleaving the semiconductor in the junction region. Although the literature on perovskite-based Schottky diodes is limited, a study reported an ideality factor of 7.09 in a Pb-based perovskite Schottky diode.[49,50] The barrier height $\varnothing_B$ was found to be 0.287 eV. But this

Table 2 FTIR assignments for oleic acid, oleylamine and Cs$_2$ZnBr$_4$ nanocrystals

Assignment	OLA	OA	Cs$_2$ZnBr$_4$
=C–H	715 cm^{-1}	715 cm^{-1}	715 cm^{-1}
C=C	958 cm^{-1}	926 cm^{-1}	974 cm^{-1}
C–H	1477 cm^{-1}, 2837 cm^{-1}, 2935 cm^{-1}	1477 cm^{-1}, 2837 cm^{-1}, 2934 cm^{-1}	1379 cm^{-1}, 1477 cm^{-1}, 2837 cm^{-1}, 2935 cm^{-1}
C–O	—	1265 cm^{-1}	—
C=O		1719 cm^{-1}	
N–H	1606 cm^{-1}	—	1590 cm^{-1}, 3225 cm^{-1}

Table 3 NMR assignments for oleic acid, oleylamine and Cs$_2$ZnBr$_4$ nanocrystals

Compound	^{1}H NMR (δ ppm)	^{13}C NMR (δ ppm)
OLA	–CH$_3$ (0.82–0.85), –CH$_2$– (1.12–1.25), –CH$_2$–CH=CH–CH$_2$– (1.90–1.97), –NH$_2$ (1.37–1.40), –CH$_2$–NH$_2$ (2.61–2.64), CH=CH (5.33–5.36)	–CH$_3$ (22.78), –CH$_2$– (27.00–34.02), –CH$_2$–NH$_2$ (42.39), CH=CH (129.91–130.20)
OA	–CH$_3$ (0.87–0.89), –CH$_2$– (1.27–2.02), –CH$_2$–C=O (2.33–2.36), CH=CH (5.33–5.36)	–CH$_3$ (14.29), –CH$_2$– (22.88–34.27), CH=CH (129.91–130.20), C=O (180.46)
Cs$_2$ZnBr$_4$	–CH$_3$ (0.92–0.94), –CH$_2$ (1.97), CH$_3$ toluene (2.10), –CH$_2$–NH$_2$ (2.22–2.23), CH=CH (5.50), CH toluene (6.98–7.18)	–CH$_3$ (18), CH toluene (122.5 & 125.5), CH=CH (127), C toluene (137)
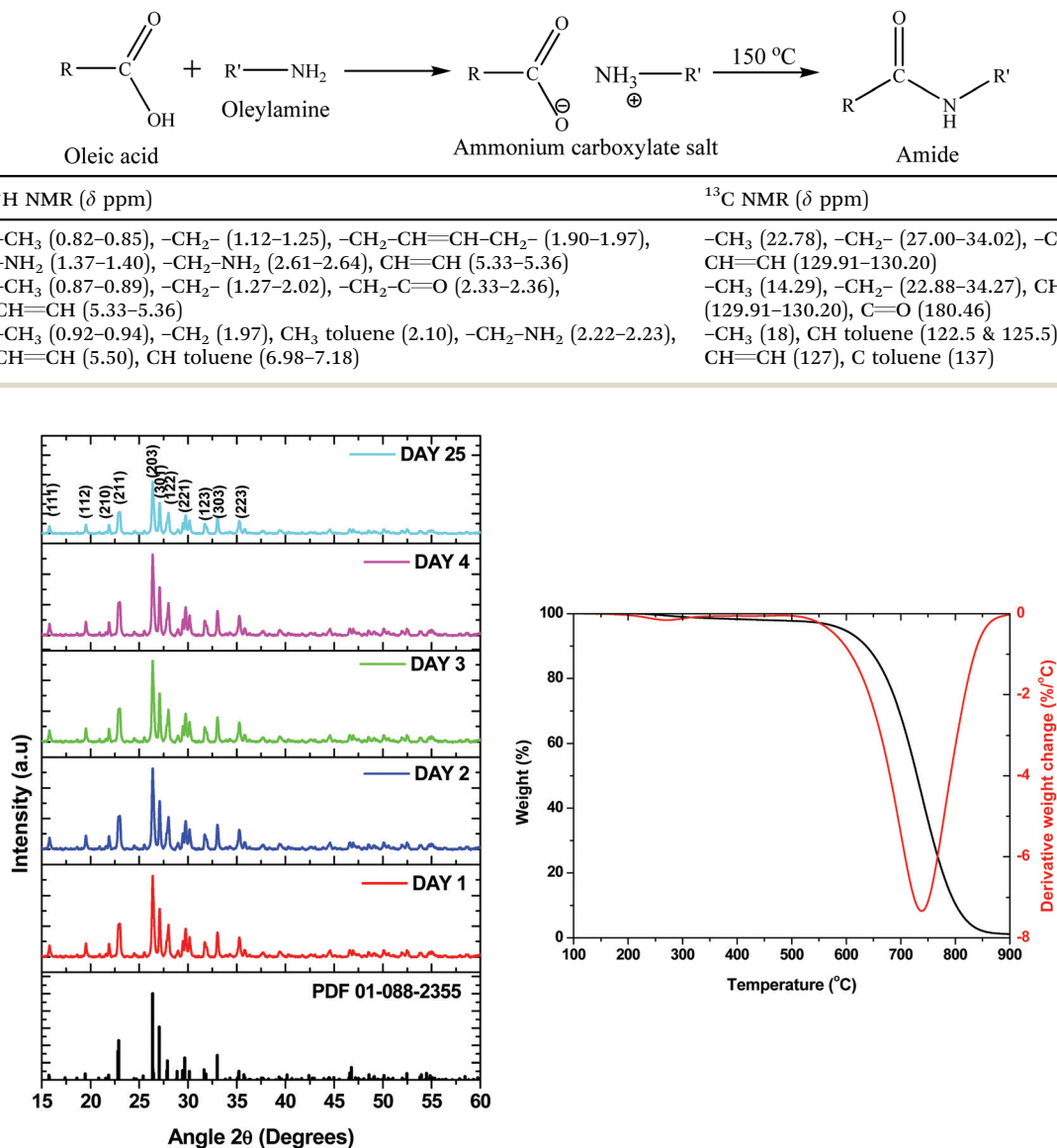
Fig. 9 Stability study of Cs$_2$ZnBr$_4$ nanocrystals synthesized at 160 °C for 1 min using (a) XRD and (b) TGA (day 25 sample).

method only works for diodes with low series resistance, which can be neglected in the low forward region of the *I–V* curve, which in the case of our diode it seems as if the series resistance cannot be ignored due to the high *n* and $\varnothing_B$ values.

Using Cheung's method, *n*, $\varnothing_B$ and R_s can be evaluated. The forward bias current–voltage characteristics due to thermionic emission of a Schottky barrier diode with series resistance can be expressed as Cheung's functions:[51]

$$\frac{\mathrm{d}V}{\mathrm{d}\mathrm{Ln}I} = n\frac{kT}{q} + IR_s \tag{5}$$
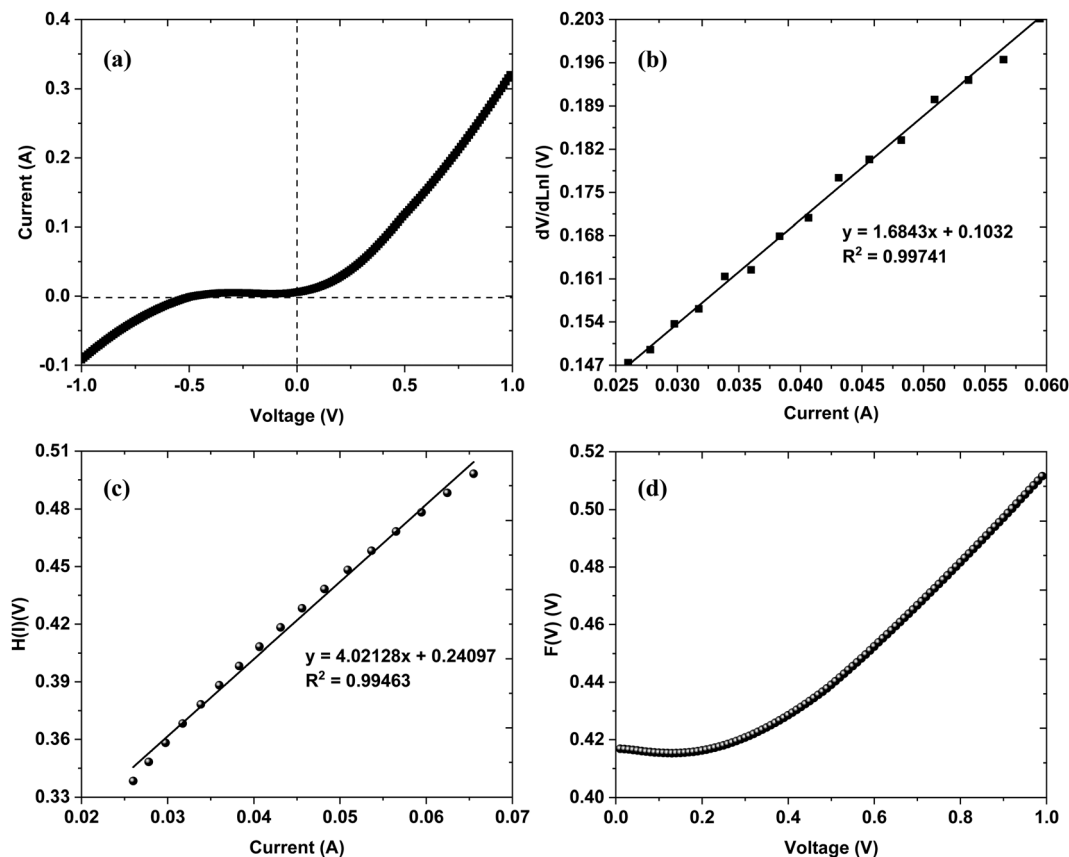
Fig. 10 (a) $I–V$, (b) $dV/dLnI–I$, (c) $H(I)–I$ and (d) $F(V)–V$ characteristics of the Au/Cs$_2$ZnBr$_4$ Schottky diode at the temperature of 298 K in the dark.

$$H(I) = V - n\frac{kT}{q}\text{Ln}\left(\frac{1}{SA^{*2}}\right) \qquad (6)$$

$$H(I) = n\varnothing_B + IR_s \qquad (7)$$

From a straight line plot (Fig. 10) of $dV/dLnI$ vs. I, n, and R_s can be calculated from the slope and the y-intercept using eqn (4). From Cheung's function, n, and R_s were found to be 4.018 and 1.684 Ω, respectively. The n value and the $I–V$ data are then used to determine $H(I)$. Using eqn (6), $\varnothing_B$ and R_s were found to be 0.059 eV and 4.021 Ω, respectively. Combining eqn (4) and (6), the average series resistance was found to be 2.852 Ω. Comparatively, a Schottky diode based on Pb perovskite was fabricated and R_s of 169.2 kΩ was obtained.[52] The series resistance is one of the parasitic resistances that influence the I-V characteristics of a Schottky diode and the determination of this parameter provides information about the performance of the Schottky device. Although there is no standard limit for R_s, however, low R_s is required for efficient solar cell performance.[53] Also, when the series resistance is high, obtaining the diode parameters, especially the determination of the barrier height becomes challenging.[54] The Schottky barrier height $\varnothing_B$ is a reflection of the energy position between the semiconductor's band edge and the metal's Fermi level where the level of the energy mismatch is indicated by the magnitude of the barrier height.[55] Since the flow of current across the metal-semiconductor junction is contingent

on the magnitude of $\varnothing_B$, the electrical properties can be confirmed after determination of $\varnothing_B$.

Furthermore, Norde proposed an alternative method to determine the values of the series resistance and the barrier height.[56] This method is employed because high series resistance can hinder an accurate evaluation of the barrier height from the standard Ln$I–V$ plot. The Norde method can be expressed as follows:

$$F(V) = \frac{V}{\gamma} - \frac{kT}{q}\text{Ln}\left(\frac{I}{SA^*T^2}\right) \qquad (8)$$

where γ is the first integer greater than n, I the current obtained from $I–V$. In this study, γ is taken to be 5. The barrier height and series resistance can be obtained from eqn (8) and (9).

$$\varnothing_B = F(V_0) + \frac{V_0}{\gamma} - \frac{kT}{q} \qquad (9)$$

$$R_s = \frac{kT(\gamma - n)}{qI} \qquad (10)$$

The barrier height and series resistance values were determined as 0.191 eV and 1.769 Ω, respectively. The values from Norde's functions are different from Cheung's methods, probably because Cheung's functions are only executed for the nonlinear region of the forward bias $I–V$ curve, while Norde's functions are executed for the whole forward bias region of the $I–V$ curve of the diode.

Table 4 Diode parameters obtained from the *I–V* data

No.	Method	Ideality factor, n	Barrier height, $\varnothing_B$	Series resistance, R_s (Ω)
1	Ln*I–V*	9.629	0.287 eV	—
2	d*V*/dLn*I–I*	4.018	—	1.684
3	*H*(*I*)–*I*	—	0.059 eV	4.021
4	*F*(*V*)–*V*	—	0.191 eV	1.769

The diode parameters extracted using different methods from the experimental *I–V* data are summarized in Table 4. The high ideality factor suggests that the fabrication of the diode requires further work, nevertheless, the rectification of the graph and reasonable current, suggests that Cs_2ZnBr_4 is a suitable candidate for use in solar cells especially as a potential material for hole or electron transport.

4. Conclusions

2D hybrid Cs_2ZnBr_4 perovskite nanocrystals were synthesized using the colloidal method. Varying the temperature and time resulted in a change in particle size and morphology. This inevitably resulted in varied optical properties. The optimum temperature and time were 160 °C and 1 min. The surface chemistry of the optimum sample was studied using XPS, FT-IR, and NMR techniques. XPS confirmed the composition of Cs_2ZnBr_4 and capping of the nanocrystals. The C 1s high-resolution spectrum shows oxygenated carbon species; however, it was not conclusive whether these were from the oleic acid or the oxidation of the surface. From FT-IR and NMR studies, oleylamine was confirmed as the only ligand capping the nanocrystals. The role of oleic acid was therefore limited to forming a more robust cesium oleate precursor. From XRD and TGA data, the particles were found to be still stable after 25 days. The optimum sample was then used as a semiconductor in a Schottky barrier diode. The ideality factor, barrier height and series resistance were determined using the traditional thermionic emission theory of a Schottky barrier, the modified Cheung's and Norde's functions. Notably, very high ideality factor values were obtained suggesting poor construction of the interface.

Conflicts of interest

There are no conflicts to declare.

Acknowledgements

References

1 National Renewable Energy Laboratory (NREL).

2 J. Burschka, N. Pellet, S.-J. Moon, R. Humphry-Baker, P. Gao, M. K. Nazeeruddin and M. Grätzel, *Nature*, 2013, **499**, 316–319.

3 D. Wang, M. Wright, N. K. Elumalai and A. Uddin, *Sol. Energy Mater. Sol. Cells*, 2016, **147**, 255–275.

4 J. Y. Woo, Y. Kim, J. Bae, T. G. Kim, J. W. Kim, D. C. Lee and S. Jeong, *Chem. Mater.*, 2017, **29**, 7088–7092.

5 G. E. Eperon, G. M. Paternò, R. J. Sutton, A. Zampetti, A. A. Haghighirad, F. Cacialli and H. J. Snaith, *J. Mater. Chem. A*, 2015, **3**, 19688–19695.

6 M. Kim, T. K. Lee, I. W. Choi, H. W. Choi, Y. Jo, J. Lee, G.-H. Kim, S. K. Kwak and D. S. Kim, *Sustainable Energy Fuels*, 2020, **4**, 3753–3763.

7 A. S. Prasad, *Adv. Nutr.*, 2013, **4**, 176–190.

8 Y. Long, C. Wang, X. Liu, J. Wang, S. Fu, J. Zhang, Z. Hu and Y. Zhu, *J. Mater. Chem. C*, 2021, **9**, 2145–2155.

9 J. Jin, H. Li, C. Chen, B. Zhang, L. Xu, B. Dong, H. Song and Q. Dai, *ACS Appl. Mater. Interfaces*, 2017, **9**, 42875–42882.

10 V. Naresh and N. Lee, *ACS Appl. Nano Mater.*, 2020, **3**, 7621–7632.

11 L. Mao, C. C. Stoumpos and M. G. Kanatzidis, *J. Am. Chem. Soc.*, 2019, **141**, 1171–1190.

12 C. C. Stoumpos and M. G. Kanatzidis, *Acc. Chem. Res.*, 2015, **48**, 2791–2802.

13 C. C. Stoumpos, C. D. Malliakas and M. G. Kanatzidis, *Inorg. Chem.*, 2013, **52**, 9019–9038.

14 L. Protesescu, S. Yakunin, M. I. Bodnarchuk, F. Krieg, R. Caputo, C. H. Hendon, R. X. Yang, A. Walsh and M. V. Kovalenko, *Nano Lett.*, 2015, **15**, 3692–3696.

15 Y. Bekenstein, B. A. Koscher, S. W. Eaton, P. Yang and A. P. Alivisatos, *J. Am. Chem. Soc.*, 2015, **137**, 16008–16011.

16 H. Tsai, W. Nie, J.-C. Blancon, C. C. Stoumpos, R. Asadpour, B. Harutyunyan, A. J. Neukirch, R. Verduzco, J. J. Crochet and S. Tretiak, *Nature*, 2016, **536**, 312–316.

17 B. Morosin and E. C. Lingafelter, *Acta Crystallogr.*, 1959, **12**, 744–745.

18 P. Cheng, L. Feng, Y. Liu, D. Zheng, Y. Sang, W. Zhao, Y. Yang, S. Yang, D. Wei, G. Wang and K. Han, *Angew. Chem., Int. Ed.*, 2020, **59**, 21414–21418.

19 D. Zhu, M. L. Zaffalon, V. Pinchetti, R. Brescia, F. Moro, M. Fasoli, M. Fanciulli, A. Tang, I. Infante, L. De Trizio, S. Brovelli and L. Manna, *Chem. Mater.*, 2020, **32**, 5897–5903.

20 V. K. LaMer and R. H. Dinegar, *J. Am. Chem. Soc.*, 1950, **72**, 4847–4854.

21 L. F. E. Machogo, P. Tetyana, R. Sithole, S. S. Gqoba, N. Phao, M. Airo, P. M. Shumbula, M. J. Moloto and N. Moloto, *Appl. Surf. Sci.*, 2018, **456**, 973–979.

22 N. Moloto, M. J. Moloto, N. J. Coville and S. Sinha Ray, *J. Cryst. Grow.*, 2009, **311**, 3924–3932.

23 A. A. Belik, S. Y. Stefanovich, B. I. Lazoryak and E. Takayama-Muromachi, *Chem. Mater.*, 2006, **18**, 1964–1968.

24 N. Pradhan, D. Reifsnyder, R. Xie, J. Aldana and X. Peng, *J. Am. Chem. Soc.*, 2007, **129**, 9500–9509.

25 S. Govindraju, M. P. Kalenga, M. Airo, M. J. Moloto, L. M. Sikhwivhilu and N. Moloto, *Opt. Mater.*, 2014, **38**, 310–313.

26 J. Butkus, P. Vashishtha, K. Chen, J. K. Gallaher, S. K. K. Prasad, D. Z. Metin, G. Laufersky, N. Gaston, J. E. Halpert and J. M. Hodgkiss, *Chem. Mater.*, 2017, **29**, 3644–3652.

27 S. T. Gentry, S. F. Kendra and M. W. Bezpalko, *J. Phys. Chem. C*, 2011, **115**, 12736–12741.

28 N. T. K. Thanh, N. Maclean and S. Mahiddine, *Chem. Rev.*, 2014, **114**, 7610–7630.

29 C. C. Yec and H. C. Zeng, *J. Mater. Chem. A*, 2014, **2**, 4843–4851.

30 S. G. Kwon and T. Hyeon, *Small*, 2011, **7**, 2685–2702.

31 P. Sahu and B. L. V. Prasad, *Langmuir*, 2014, **30**, 10143–10150.

32 T. van Westen and R. D. Groot, *Cryst. Growth Des.*, 2018, **18**, 4952–4962.

33 C. Yang, Z. F. Zhou, J. W. Li, X. X. Yang, W. Qin, R. Jiang, N. G. Guo, Y. Wang and C. Q. Sun, *Nanoscale*, 2012, **4**, 1304–1307.

34 D. Segets, J. M. Lucas, R. N. Klupp Taylor, M. Scheele, H. Zheng, A. P. Alivisatos and W. Peukert, *ACS Nano*, 2012, **6**, 9021–9032.

35 T. Vossmeyer, L. Katsikas, M. Giersig, I. G. Popovic, K. Diesner, A. Chemseddine, A. Eychmueller and H. Weller, *J. Phys. Chem.*, 1994, **98**, 7665–7673.

36 M. Yang, T. Zhang, P. Schulz, Z. Li, G. Li, D. H. Kim, N. Guo, J. J. Berry, K. Zhu and Y. Zhao, *Nat. Commun.*, 2016, **7**, 12305.

37 S. Li, L. Hu, C. Zhang, Y. Wu, Y. Liu, Q. Sun, Y. Cui, Y. Hao and Y. Wu, *J. Mater. Chem. C*, 2020, **8**, 2425–2435.

38 X. Cao, L. Zhi, Y. Li, F. Fang, X. Cui, L. Ci, K. Ding and J. Wei, *ACS Appl. Energy Mater.*, 2018, **1**, 868–875.

39 R. K. Sithole, L. F. E. Machogo, M. A. Airo, S. S. Gqoba, M. J. Moloto, P. Shumbula, J. V. Wyk and N. Moloto, *New J. Chem.*, 2018, **42**, 3042–3049.

40 J. Escard, G. Mavel, J. E. Guerchais and R. Kergoat, *Inorg. Chem.*, 1974, **13**, 695–701.

41 C. Rocks, V. Svrcek, P. Maguire and D. Mariotti, *J. Mater. Chem. C*, 2017, **5**, 902–916.

42 R. Seals, R. Alexander, L. T. Taylor and J. G. Dillard, *Inorg. Chem.*, 1973, **12**, 2485–2487.

43 J. Sharma and Z. Iqbal, *Chem. Phys. Lett.*, 1978, **56**, 373–376.

44 G. Almeida, L. Goldoni, Q. Akkerman, Z. Dang, A. H. Khan, S. Marras, I. Moreels and L. Manna, *ACS Nano*, 2018, **12**, 1704–1711.

45 H. Sun, Z. Li, L. Kong, B. Wang, C. Zhang, Q. Yuan, S. Huang, Y. Liu and L. Li, *Chem. Commun.*, 2018, **54**, 9345–9348.

46 E. H. Rhoderick and R. H. Williams, *Metal-Semiconductor Contacts*, Clarendon Press, 1988.

47 S. Colella, E. Mosconi, P. Fedeli, A. Listorti, F. Gazza, F. Orlandi, P. Ferro, T. Besagni, A. Rizzo and G. Calestani, *Chem. Mater.*, 2013, **25**, 4613–4618.

48 S. Khan, S. Halder, A. Dey, B. Dutta, P. P. Ray and S. Chattopadhyay, *New J. Chem.*, 2020, **44**, 11622–11630.

49 L. Chen, J. Deng, H. Gao, Q. Yang, G. Wang, L. Kong, M. Cui and Z. Zhang, *J. Mater. Sci.: Mater. Electron.*, 2016, **27**, 4275–4280.

50 C.-H. Lin, T.-Y. Li, B. Cheng, C. Liu, C.-W. Yang, J.-J. Ke, T.-C. Wei, L.-J. Li, A. Fratalocchi and J.-H. He, *Nano Energy*, 2018, **53**, 817–827.

51 S. Cheung and N. Cheung, *Appl. Phys. Lett.*, 1986, **49**, 85–87.

52 P. A. Shaikh, D. Shi, J. R. D. Retamal, A. D. Sheikh, M. A. Haque, C.-F. Kang, J.-H. He, O. M. Bakr and T. Wu, *J. Mater. Chem. C*, 2016, **4**, 8304–8312.

53 F. Fabregat-Santiago, G. Garcia-Belmonte, I. Mora-Seró and J. Bisquert, *Phys. Chem. Chem. Phys.*, 2011, **13**, 9083–9118.

54 E. Karagöz, S. F. Varol, S. Sayın and Z. Merdan, *Phys. Chem. Chem. Phys.*, 2018, **20**, 30502–30513.

55 A. E.-D. S. Hafez and M. Abd El-Latif, *ISRN Electron.*, 2013, **2013**, e528094.

56 H. Norde, *J. Appl. Phys.*, 1979, **50**, 5052–5053.